



# UiO-66-based metal organic frameworks for the photodegradation of acetaminophen under simulated solar irradiation

Y.L. Wang<sup>a</sup>, S. Zhang<sup>b</sup>, Y.F. Zhao<sup>b</sup>, J. Bedia<sup>a</sup>, J.J. Rodriguez<sup>a</sup>, C. Belver<sup>a,\*</sup>

<sup>a</sup> Department of Chemical Engineering, Universidad Autonoma de Madrid, Cantoblanco, 28049 Madrid, Spain

<sup>b</sup> State Key Laboratory of Luminescent Materials and Devices, and Guangdong Provincial Key Laboratory of Fiber Laser Materials and Applied Techniques, South China University of Technology, 510641 Guangzhou, China

## ARTICLE INFO

Editor: Dr. GL Dotto

### Keywords:

Metal organic framework  
UiO-66  
Solar photocatalytic degradation  
Acetaminophen  
Continuous reaction

## ABSTRACT

This work reports the solvothermal synthesis of UiO-66-based MOFs with three different ligands and its application to the breakdown of aqueous acetaminophen under simulated sunlight. This pharmaceutical is a representative contaminant of emerging concern that enters water bodies mainly through wastewater treatment plant discharges. The synthesis approach of the MOFs was fitted using a zirconium alkoxide as metal cluster precursor and 2-aminoterephthalic and 2,5-dihydroxyterephthalic acids as ligands to prepare UiO-66-NH<sub>2</sub> and UiO-66-(OH)<sub>2</sub> MOFs, respectively. These new MOFs have enhanced visible light harvesting and narrower band gap than the UiO-66. Among all, UiO-66-NH<sub>2</sub> yielded the highest removal of acetaminophen under simulated solar irradiation in batch test. The activity and stability of UiO-66-NH<sub>2</sub> were demonstrated for the first time in a continuous flow test, where stable performance was observed upon 30 h on stream. The degradation pathway of acetaminophen was elucidated based on coupling, ring-opening, and oxidation reactions. DFT calculation confirmed that the indirect semiconductor behavior of UiO-66-NH<sub>2</sub> upon light excitation occurred through ligand-ligand charge transfer. Overall, promising UiO-66-based MOFs photocatalysts were obtained for effective degradation of acetaminophen with the assistance of solar light.

## 1. Introduction

Pharmaceuticals and personal care products (PPCPs) have received widespread attention as contaminants of emerging concern because of their persistence and bioaccumulation in the ecosystem [1]. Whether through drinking water or consuming aquatic organisms, exposition to PPCPs represent a threat to human health. With long-term exposure, they can cause cancer, endocrine disorders, antibiotic resistance, and several chronic diseases [2]. Acetaminophen (ACE) is a representative PPCP widely used as pain reliever. It enters water bodies mainly through wastewater treatment plants, causing a significant negative impact on the environment due to its recalcitrant character [3]. Therefore, it is essential to develop technologies providing cost-effective solutions to that environmental problem. Various methods have been analyzed for ACE removal, including adsorption and advanced oxidation processes (AOPs) (Fenton reaction methods, sulfate radical (SO<sub>4</sub><sup>•-</sup>)-mediated oxidations, and photocatalysis) [4–6]. Adsorption has the advantages of simplicity, but the main drawback of not being a destructive method [7]. AOPs involve highly reactive *in situ* generated oxygen species that can

convert organic pollutants into less toxic products. Under proper conditions, those processes can mineralize organic matter into CO<sub>2</sub> and H<sub>2</sub>O [8]. Among the different AOPs, photocatalysis represents an environmentally friendly technology, mainly when solar irradiation can be used. Although traditional photocatalysts, such as TiO<sub>2</sub>, ZnO and Fe<sub>2</sub>O<sub>3</sub>, have made significant achievements in the field of photocatalytic degradation of pollutants, their technical application is still limited by the lack of visible light absorption capacity and the easy recombination of photoinduced electrons and holes [9].

More recently, metal organic frameworks (MOFs) have received growing attention as photocatalysts due to their tunable porous and open topological structure, ultra-large surface areas, and abundant active sites [10]. Furthermore, the ordered structure of MOFs can be adjusted by changing the metal centers and modifying the organic ligands with different functional groups at the molecular level to improve their performance for specific applications [11,12]. Like metal oxide semiconductors, MOFs can also be photoexcited by light to generate electron-hole pairs [13]. The organic ligands have strong light absorption capacity due to the presence of large  $\pi$ -conjugated systems [14].

\* Corresponding author.

E-mail address: [carolina.belver@uam.es](mailto:carolina.belver@uam.es) (C. Belver).

<https://doi.org/10.1016/j.jece.2021.106087>

Received 20 May 2021; Received in revised form 9 July 2021; Accepted 16 July 2021

Available online 21 July 2021

2213-3437/© 2021 The Author(s).

Published by Elsevier Ltd.

This is an open access article under the CC BY-NC-ND license

(<http://creativecommons.org/licenses/by-nc-nd/4.0/>).

Due to these characteristics, MOFs are being widely analyzed for photocatalytic abatement of water pollutants [15]. However, some MOFs are prone to hydrolysis in the presence of water due to the weak coordinate bond between metal ions and oxygen, which causes irreversible collapse of the pore structure [16]. The instability of many metal organic framework materials hinders further real applications. UiO-66 is one of the MOFs with higher thermal stability, and good chemical resistance to water due to the strong coordination bonds between the strong-acid-strong-base interactions of the Zr(IV) atoms and carboxylate oxygens [17]. Although UiO-66 has many advantages, it needs ultraviolet radiation to be activated, due to its relatively wide band gap ( $\sim 3.60$  eV) [18]. To overcome this limitation, many studies are devoted to synthesizing modified UiO-66-based MOFs with narrower band gap values to get an effective response under visible light so that solar radiation can be used.

Among the alternatives, the introduction of different functional groups on the organic ligand is a common way to adjust the band gap of MOFs in order to enhance visible light harvesting. Chen et al. [19] prepared UiO-66-(SO<sub>3</sub>)<sub>2</sub>, UiO-66-(SH)<sub>2</sub> and UiO-66-(SCH<sub>3</sub>)<sub>2</sub> with lower band gaps, 2.80, 3.02 and 3.22 eV, respectively, functionalizing the UiO-66 ligand with different sulfur-containing functional groups. Mu et al. [20] synthesized a series of isostructural UiO-66, UiO-66-Br, UiO-66-NH<sub>2</sub>, UiO-66-(SH)<sub>2</sub> and UiO-66-(OH)<sub>2</sub> catalysts, with band gap values between 3.91 and 2.69 eV, for a dye degradation under visible light. This study suggested  $\text{—NH}_2$  as the most effective functional group for narrowing the band gap. However, the use of these MOFs for the removal of emerging contaminants in continuous tests using solar radiation has not been studied previously.

In this study, UiO-66-based MOFs with organic ligands containing different functional groups were synthesized in a single-step by a solvothermal method, using for the first-time zirconium butoxide as precursor of the metal clusters. The resulting MOFs have been tested as photocatalysts for acetaminophen degradation under simulated solar irradiation. The effects of the functional groups on the properties of the resulting MOFs and their catalytic behavior were studied, highlighting as novelty the performance in a continuous degradation test upon 30 h on stream. DFT calculations have been performed to know the contribution of different orbitals to the VBM and CBM and to infer the electron transfer mechanism.

## 2. Experimental

### 2.1. Reagents

Zirconium butoxide (Zr(OC<sub>4</sub>H<sub>9</sub>)<sub>4</sub>, 80%), terephthalic acid (TA) (C<sub>8</sub>H<sub>6</sub>O<sub>4</sub>, 98%), 2-aminoterephthalic acid (2ATA) (C<sub>8</sub>H<sub>7</sub>NO<sub>4</sub>, 99%), 2,5-dihydroxyterephthalic acid (2,5HA) (C<sub>8</sub>H<sub>6</sub>O<sub>6</sub>, 98%), formic acid (HCOOH,  $\geq 95\%$ ), acetaminophen (ACE) (C<sub>8</sub>H<sub>9</sub>NO<sub>2</sub>,  $\geq 99\%$ ), methanol (CH<sub>3</sub>OH,  $\geq 99.9\%$ ), acetic acid (CH<sub>3</sub>COOH,  $\geq 99\%$ ), benzoquinone (p-BQ) (C<sub>6</sub>H<sub>4</sub>O<sub>2</sub>,  $\geq 98\%$ ), silver nitrate, (AgNO<sub>3</sub>,  $\geq 99\%$ ) and triethylamine (C<sub>6</sub>H<sub>15</sub>N, 98%) were purchased from Sigma-Aldrich Corporation. N,N-dimethylformamide (C<sub>3</sub>H<sub>7</sub>NO,  $\geq 99.8\%$ ) and 2-propanol (C<sub>3</sub>H<sub>8</sub>O, 99.7%) were acquired from AppliChem. All these chemical reagents were of analytical grade and used without further purification.

### 2.2. Preparation of metal-organic frameworks

The synthesis of UiO-66 was adapted from the literature [21]. Terephthalic acid (1.5 mmol) and zirconium butoxide (1.5 mmol) were dissolved in DMF (20 mL) in a 100 mL Schott bottle. The solution was placed in an ultrasonic bath until it was totally transparent. Then 10 mL formic acid were added into the above solution as modulator and placed again in an ultrasonic bath. After sealing the Schott bottle, it was introduced into the oven (Mettler 30-1060, Germany) and set at 120 °C for 24 h. Then, the sample was left to cool down, and washed 3 times by centrifugation (Digicen 21R, Spain) with DMF to extract any

residual reactant and subsequently with absolute methanol by centrifugation another 3 times to remove DMF. Before washing with DMF and methanol, the powder was soaked in fresh DMF for 1 h and in methanol for 24 h. The collected powder was vacuum-dried at 70 °C (SVOV-30, Germany) overnight to get the final UiO-66 powder. UiO-66-NH<sub>2</sub> and UiO-66-(OH)<sub>2</sub> MOFs were synthesized following the same procedure but with different organic ligands, 2-aminoterephthalic acid (2ATA) and 2,5-dihydroxyterephthalic acid (2,5HT), respectively.

### 2.3. Characterization

X-ray diffraction (XRD) patterns were recorded in the  $2\theta$  range of 5–50° at a scan rate of 1.5° min<sup>−1</sup>, by using a Bruker D8 diffractometer with a Cu-K $\alpha$  ( $\lambda = 0.15406$  nm) radiation source. The porous texture of the samples was characterized by N<sub>2</sub> adsorption-desorption at  $-196$  °C, using a micromeritics TriStar 123 apparatus. The specific surface area ( $S_{\text{BET}}$ ) was calculated by the Brunauer-Emmett-Teller (BET) method. The microporous volume ( $V_{\text{MP}}$ ) and so-called external or non-microporous surface area ( $S_{\text{EXT}}$ ) were determined with the t-plot method. The total pore volume ( $V_{\text{P}}$ ) was estimated from the amount of nitrogen adsorbed at a relative pressure ( $P/P_0$ ) of 0.99. All samples were outgassed under vacuum at 120 °C overnight prior to the measurements. The UV–visible absorbance spectra of the photocatalysts were obtained using a Japan Shimadzu 2501PC UV–vis spectrophotometer with BaSO<sub>4</sub> as reference in the wavelength range of 200–800 nm. The absorbance data were used to calculate the band gap of the samples by the Tauc plot method, considering them as indirect semiconductors. Scanning electron microscopy (SEM) images were obtained by means of a Quanta 3D FEG (FEI) apparatus. A Bruker IFS 66 v/s infrared spectrometer was used for the Fourier transform infrared (FTIR) spectra in the 4000–400 cm<sup>−1</sup> wavenumber range with a resolution of 2 cm<sup>−1</sup>. Photoluminescence spectra (PL) of the samples were recorded by a FL920 fluorescence spectrometer (Edinburgh Instruments Ltd) equipped with a 450 W xenon lamp. Mott-Schottky measurements were performed on a Metrohm Autolab electrochemical workstation. Typically, 1 mg of solid was suspended into 10 mL ethanol and 10  $\mu$ L Nafion solution. The resulting suspension was supported on a glassy carbon-coated working electrode. The measurements were performed in a three-electrodes system with Pt wire and Ag/AgCl as auxiliary and reference electrodes, respectively. The electrolyte was 0.1 M Na<sub>2</sub>SO<sub>4</sub> solution. The Mott-Schottky plot measurements were recorded at 1000, 2000 and 3000 Hz. Total organic carbon (TOC) was measured with a Shimadzu TOC-L analyzer. River water sample was taken from Valdebebas stream (Madrid, Spain) and filtered to remove suspended particles.

### 2.4. Photocatalytic tests

The degradation test of ACE in aqueous solution was performed at 25 °C in a Pyrex glass jacketed reactor (500 mL) under irradiation in a solar simulator chamber equipped with a Xe lamp (Suntest XLS+, ATLAS) and a 320 nm cut-off filter. The light intensity was set at 600 W m<sup>−2</sup>. A suspension of the photocatalyst (250 mg L<sup>−1</sup>) in an aqueous ACE solution (150 mL, 5 mg L<sup>−1</sup>) was magnetically stirred in dark for 1 h to reach adsorption equilibrium. During the reaction, 0.45 mL samples were taken at specific times and filtered off with PTFE syringeless filters (Whatman 0.2  $\mu$ m) to separate the solid photocatalyst. ACE concentration was measured by high-performance liquid chromatography (HPLC; Shimadzu Prominence-I LC-2030C, Japan) with a diode array detector (SPDM30 A), using a C18 column (Eclipse Plus 5  $\mu$ m, Agilent). The chromatographic method used was a gradient elution, using two mobile phases of 0.1% acetic acid aqueous solution and acetonitrile at 0.7 mL min<sup>−1</sup>. The experiments were carried out by duplicate and the standard deviation was always lower than 5%.

The intermediate species from acetaminophen (ACE) degradation were identified by Liquid Chromatography coupled to Electrospray Ionization-Mass spectrometry (LC/ESI-MS). Electrospray ionization

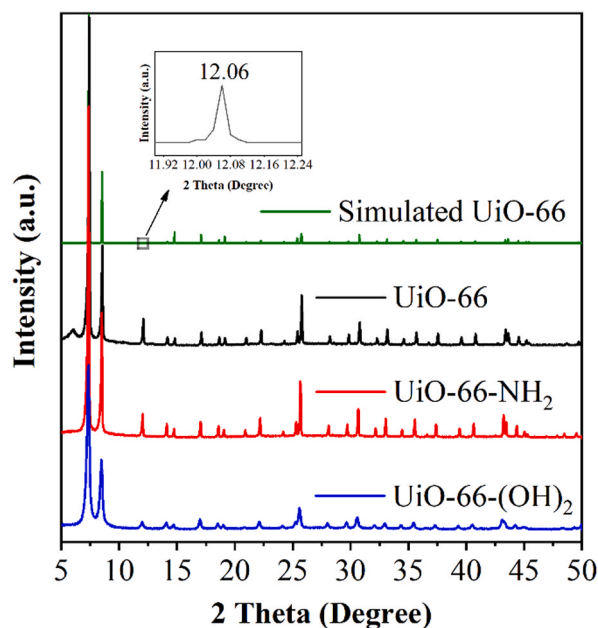


Fig. 1. XRD patterns of the synthesized MOFs.

(ESI) was acquired in positive ionization mode under the following conditions: a capillary voltage of 3500 V, dry gas flow of  $8 \text{ mL min}^{-1}$  at  $300^\circ\text{C}$ , and end plate offset of 500 V. Mass spectrometric data were collected in full scan mode of 0.1 s from 50 to 3000  $m/z$  with a collision energy of 30 eV. Short-chain carboxylic acids and inorganic ions were analyzed by ionic chromatography in a Metrohm 790 IC chromatograph, with  $250 \text{ mm} \times 4 \text{ mm}$  column (Metrosep A Supp 5), using  $\text{Na}_2\text{CO}_3/\text{NaHCO}_3$  (3.2 mM/1.0 mM) solution as anionic eluent and 100 mM sulfuric acid as anionic suppressor at  $0.7 \text{ mL min}^{-1}$ .

## 2.5. Computational methods

The first-principles electronic structure calculation was carried out by MedeA-VASP, a package based on density functional theory (DFT). Geometry optimization and electronic structure computation of the photocatalyst was performed using the generalized gradient approximation (GGA) based Perdew-Burke-Ernzerhof (PBE) exchange-correlation functional. Default plane-wave cutoff energy was set at 400 eV. The requested k-spacing is 0.25 per Angstrom, which leads to a  $3 \times 3 \times 3$  mesh centered on the gamma point. The structures were relaxed with the energy convergence criterion set to  $1 \times 10^{-5}$  eV, ensuring that the maximum force on an atom at the end of relaxation was  $< 0.02 \text{ eV } \text{\AA}^{-1}$ .

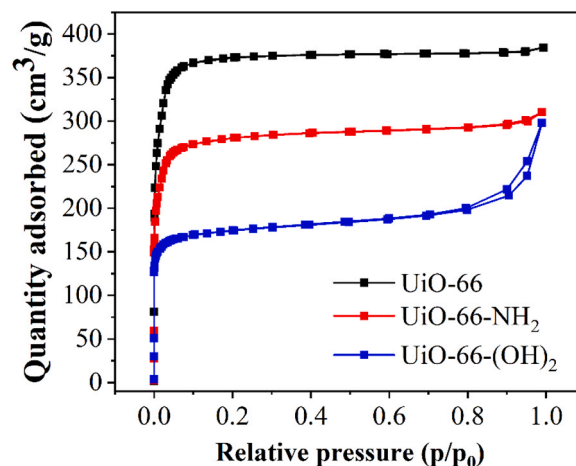


Fig. 3. Nitrogen adsorption-desorption isotherms at  $-196^\circ\text{C}$  of the synthesized MOFs.

## 3. Result and discussion

### 3.1. Characterization

Fig. 1 depicts the XRD patterns of the synthesized MOFs. All the samples show diffraction peaks at similar angles, with the most intense ones at  $2\theta$  values of  $7.4$  and  $8.5^\circ$ , in good agreement with the simulated pattern of the single crystal of UiO-66. Modified UiO-66-NH<sub>2</sub> and UiO-66-(OH)<sub>2</sub> show similar patterns to that of the original UiO-66 framework, confirming that they are topologically equivalent with the face-centered cubic lattice of the UiO-66 structure. The diffraction patterns of UiO-66-NH<sub>2</sub> and UiO-66-(OH)<sub>2</sub> correspond to those previously described in the literature [22,23]. The average crystal size ( $D$ ) was calculated by Scherrer's equation using the peak at  $7.4^\circ$ . UiO-66 and UiO-66-NH<sub>2</sub> have quite similar average crystal sizes of 73.6 and 72.1 nm, respectively, while UiO-66-(OH)<sub>2</sub> has a significantly lower value (29.7 nm), which means less crystallinity. Abid et al. [24] calculated 63.2 nm for UiO-66 crystal size, and Chen et al. [25] obtained 32.9 nm for UiO-66-(OH)<sub>2</sub>, both comparable with these of the current study. The respective chemical structures are shown in Fig. S1 of Supporting information. Fig. 2 shows characteristic SEM images of the synthesized materials. The morphology of UiO-66 shows regular octahedrons with uneven distribution, showing particle sizes between c.a. 200 nm and 1  $\mu\text{m}$ . With 2ATA as organic ligand, the MOF particles are also regular octahedrons, although with a relatively uniform size (average around 280 nm). Finally, the average size of UiO-66-(OH)<sub>2</sub> particles decreased down to 100 nm. The morphology of UiO-66 and UiO-66-NH<sub>2</sub> MOFs is like the previously reported by Zhao et al. [26]. The size and

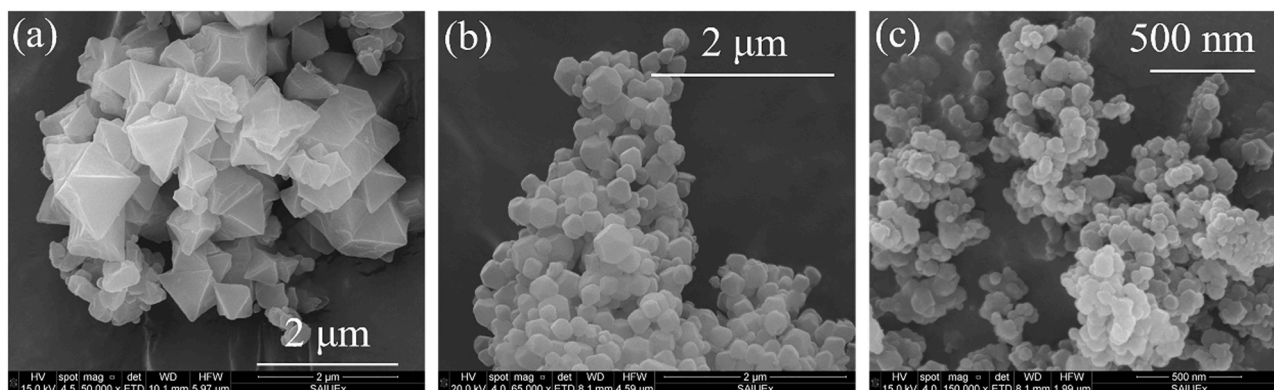


Fig. 2. SEM images of (a) UiO-66, (b) UiO-66-NH<sub>2</sub> and (c) UiO-66-(OH)<sub>2</sub>.



**Table 1**

Porous texture of the synthesized MOFs.

Sample	$S_{\text{BET}}$ ( $\text{m}^2\text{g}^{-1}$ )	$S_{\text{EXT}}$ ( $\text{m}^2\text{g}^{-1}$ )	$V_{\text{MP}}$ ( $\text{cm}^3\text{g}^{-1}$ )	$V_{\text{P}}$ ( $\text{cm}^3\text{g}^{-1}$ )	$V_{\text{MP}}/V_{\text{P}}$
UiO-66	1198	89	0.54	0.59	91.5%
UiO-66- $\text{NH}_2$	904	120	0.38	0.48	79.2%
UiO-66- $(\text{OH})_2$	567	101	0.22	0.46	47.8%

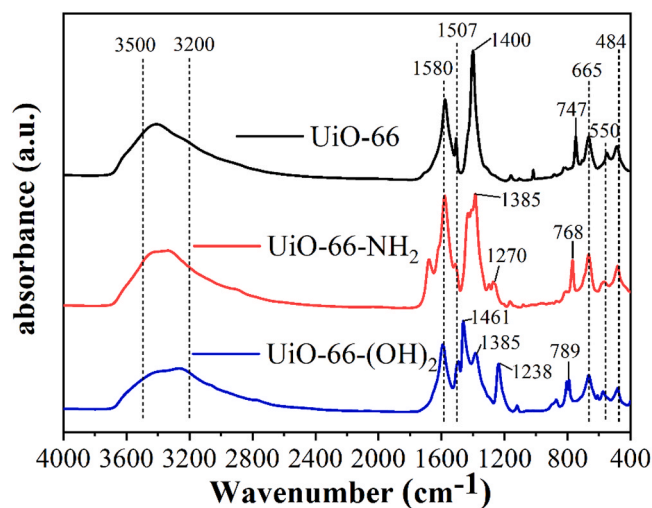


**Fig. 4.** FTIR spectra of the synthesized MOFs. (For interpretation of the references to colour in this figure, the reader is referred to the web version of this article.)

morphology of the synthesized UiO-66- $(\text{OH})_2$  agree with those obtained in previous studies as well [27,28].

Nitrogen adsorption-desorption isotherms of the synthesized MOFs are shown in Fig. 3. UiO-66 and UiO-66- $\text{NH}_2$  describe type I isotherm (IUPAC classification) characteristic of microporous solids, whereas the UiO-66- $(\text{OH})_2$  presents significantly higher relative contribution of mesoporosity, as indicated by a more pronounced slope of the horizontal-like branch with a sharpen rise beyond 0.8 relative pressure and a relatively low area hysteresis cycle. Table 1 summarizes the characterization of the porous texture of these MOFs. The presence of

functional groups in the organic ligand reduces the specific surface area of the MOF, much more evident for UiO-66- $(\text{OH})_2$ , whose BET surface area is less than one-half that of the UiO-66 MOF. Meanwhile, the functional groups affected also to the distribution of porosity. The mesoporosity contribution (assessed from the ratio of the external to BET surface area) varies from less than 8% for UiO-66 to almost 18% in UiO-66- $(\text{OH})_2$ . Regarding the pore volume, the ratio of micropore to total pore volume ( $V_{\text{MP}}/V_{\text{P}}$ , Table 1) reduces from UiO-66 to UiO-66- $(\text{OH})_2$  due to the reduction of the free volume produced by the incorporation of the new functional groups, more pronounced in the last one, with two hydroxyl groups, than for UiO-66- $\text{NH}_2$  with only one amine group [29,30].

The FTIR spectra of three MOFs are depicted in Fig. 4. The wide band at  $3400\text{ cm}^{-1}$  can be attributed to  $-\text{OH}$  stretching vibration from the absorbed water molecules [31]. All MOFs show intense bands at  $1580$  and around  $1400\text{ cm}^{-1}$ , corresponding to the asymmetric and symmetric stretching vibrations of the carboxylate groups from terephthalic ligand [32], and the weak band at  $1507\text{ cm}^{-1}$  associated to the  $\text{C}=\text{C}$  vibration of the benzene ring [33]. In the low-frequency region, the band near  $550\text{ cm}^{-1}$  is attributed to  $\text{Zr}-(\text{OC})$  asymmetric stretching vibration [34], and the vibration peaks around  $665$  and  $484\text{ cm}^{-1}$  are related to the stretching vibration of  $\text{Zr}-\text{O}_{\mu 3-\text{O}}$  and  $\text{Zr}-\text{O}_{\mu 3-\text{OH}}$  bonds of the  $\text{Zr}_6$  cluster, respectively [35]. The peaks at  $747$ ,  $768$ , and  $789\text{ cm}^{-1}$  are associated to  $\text{C}-\text{H}$  vibration in the different ligands [31]. In the case of UiO-66- $\text{NH}_2$ , the band between  $3200$  and  $3500\text{ cm}^{-1}$  is wider than that of UiO-66, probably due to the stretch vibration of the  $-\text{NH}_2$  group at  $3300\text{ cm}^{-1}$ , overlapped with the characteristic band of adsorbed water [36]. The presence of the  $-\text{NH}_2$  group is corroborated by the  $\text{N}-\text{H}$  bending vibration, observed at  $1680\text{ cm}^{-1}$  in the UiO-66- $\text{NH}_2$  spectrum. This MOF shows a characteristic  $\text{C}-\text{N}$  stretching vibration band at  $1270\text{ cm}^{-1}$ , attributed to the  $\text{C}-\text{N}$  bonds of amino groups to the benzene ring [37]. The FTIR spectrum shows that the UiO-66- $(\text{OH})_2$  has blue shifted at  $3500-3200\text{ cm}^{-1}$  which is attributed to the presence of hydroxyl functional groups [38]. This spectrum also shows strong bands at  $1461$  and  $1238\text{ cm}^{-1}$  corresponding, respectively, to bending and stretching vibrations of phenolic  $\text{C}-\text{O}-\text{H}$  groups in the ligand [24]. These results corroborate the presence of different functional groups in the synthesized MOFs.

The UV-Vis absorption spectra of the samples are depicted in Fig. 5. The absorption peaks of all samples in the vicinity of  $250\text{ nm}$  are due to the light absorption of  $\text{Zr}_6$  clusters, while the peaks at  $323$  and  $364\text{ nm}$  are associated with the amine and hydroxyl ligand groups, respectively. Thus, the energy band edges of UiO-66- $\text{NH}_2$  and UiO-66- $(\text{OH})_2$  are significantly shifted to the visible light region with enhanced light

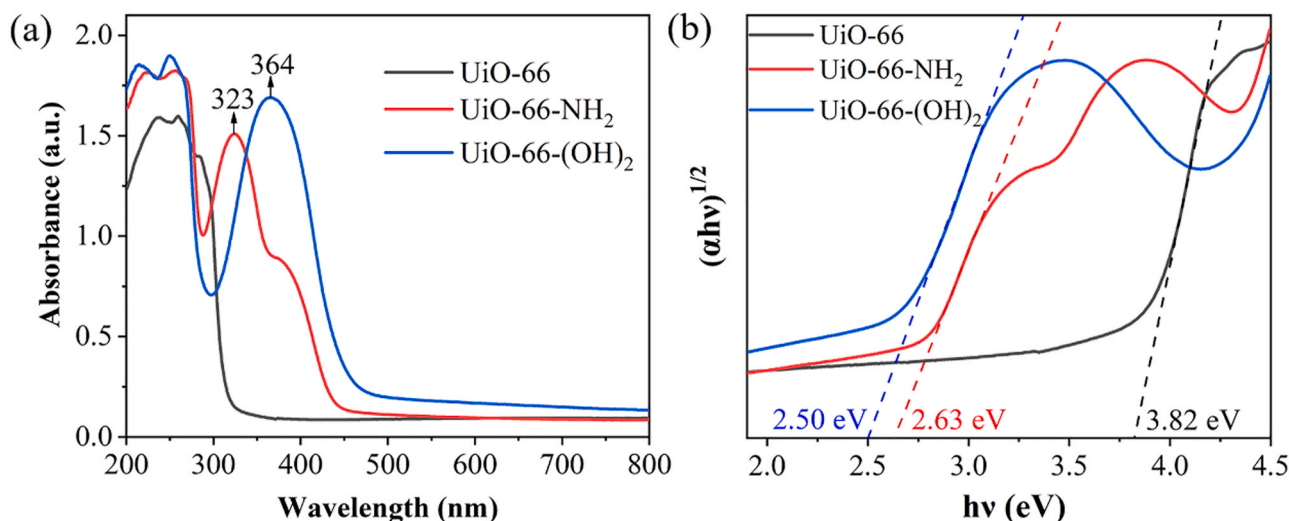


**Fig. 5.** (a) UV-vis diffuse absorbance spectra and (b) Tauc plots.

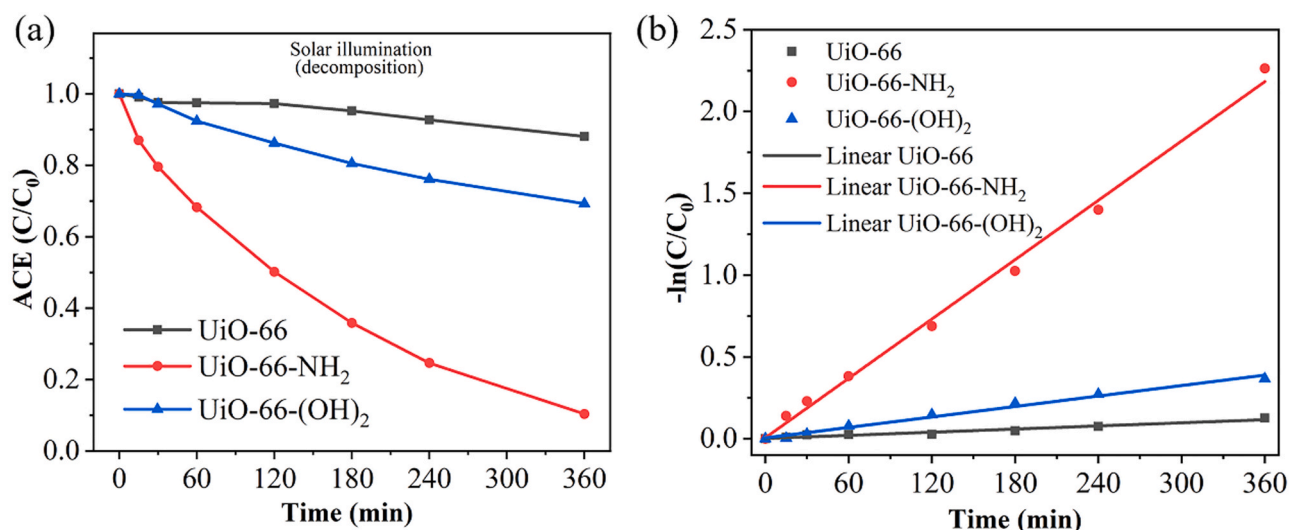


Fig. 6. (a) Solar photocatalytic degradation of acetaminophen and (b) pseudo-first-order kinetic plots (experimental points and fitting lines) ( $[ACE]_0 = 5 \text{ mg L}^{-1}$ ;  $[catalyst] = 250 \text{ mg L}^{-1}$ ; Intensity =  $600 \text{ W m}^{-2}$ ).

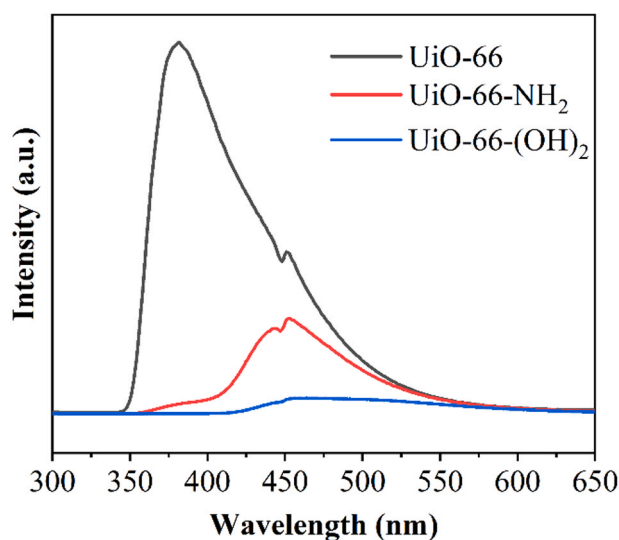


Fig. 7. PL spectra of the photocatalysts.

harvesting. Considering these MOFs as indirect semiconductors, the band gap values of the samples were calculated from the Tauc plot (Fig. 5b) of  $(\alpha h\nu)^{1/2}$  versus energy ( $h\nu$ ) [39]. The band gap values of UiO-66, UiO-66-NH<sub>2</sub> and UiO-66-(OH)<sub>2</sub> were 3.82, 2.63 and 2.50 eV, respectively, in agreement with the values reported in other works [20, 40]. These results confirm that the ligand functionalization can narrow the band gap of UiO-66. The functional groups linked to the aromatic ring acts as antenna enhancing the light harvesting.

### 3.2. Photocatalytic degradation tests

Fig. 6a shows the time course of ACE evolution upon photocatalytic reaction under solar irradiation with the MOFs. The ACE adsorption was evaluated prior to the reaction test, resulting in negligible values in all cases, less than 5%. UiO-66-NH<sub>2</sub> showed by far the best performance, allowing more than 90% ACE conversion after 6 h of irradiation. The experimental concentration vs time curves were fitted to first-order rate equation (Fig. 6b) and the values of the kinetic constant were 0.018, 0.37 and  $0.067 \text{ h}^{-1}$  for UiO-66, UiO-66-NH<sub>2</sub> and UiO-66-(OH)<sub>2</sub>, respectively. Compared with previously reported works, the value of

pseudo-first order rate constant of ACE disappearance with UiO-66-NH<sub>2</sub> is significantly higher than that obtained with ZnO/sepiolite ( $0.19 \text{ h}^{-1}$ ) [41] and like those of TiO<sub>2</sub>-based heterostructures ( $0.4$  and  $0.5 \text{ h}^{-1}$ ) [42, 43]. Higher rate constant was reported for zirconium-doped-NH<sub>2</sub>-MIL-125(Ti) MOF ( $0.73 \text{ h}^{-1}$ ) for ACE photodegradation upon the same reaction conditions [44], although this MOF showed lower stability in aqueous phase than this of the current work.

Photoluminescence (PL) measurements serve to learn on the recombination of photogenerated electron-hole pairs, so to better understand the behavior of a given material as photocatalyst. Fig. 7 shows the PL spectra of the synthesized MOFs obtained at an excitation wavelength of 300 nm. As can be seen, UiO-66 has a strong emission peak at around 376 nm [45]. Comparatively, the PL intensity of UiO-66-NH<sub>2</sub> shows a significantly decreased luminescence signal displaced to higher wavelengths (centered at 443 nm), which can be attributed to lower recombination rate of electron-hole pairs [46]. UiO-66-(OH)<sub>2</sub> shows the lowest PL intensity, suggesting the lowest recombination rate. Yao et al. reported quite similar photoluminescence spectra for UiO-66-(OH)<sub>2</sub> [47]. However, this dihydroxy-modified UiO-66 did not exhibit the best photocatalytic performance, as shown before. It should be considered that the factors determining

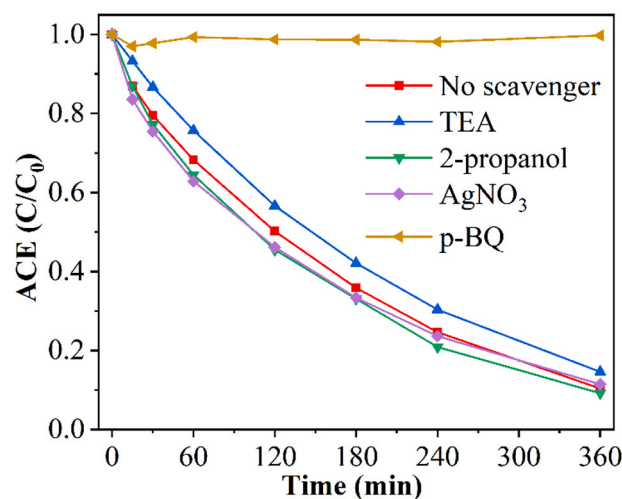


Fig. 8. Effect of different scavengers on the photocatalytic decay of ACE with UiO-66-NH<sub>2</sub>.

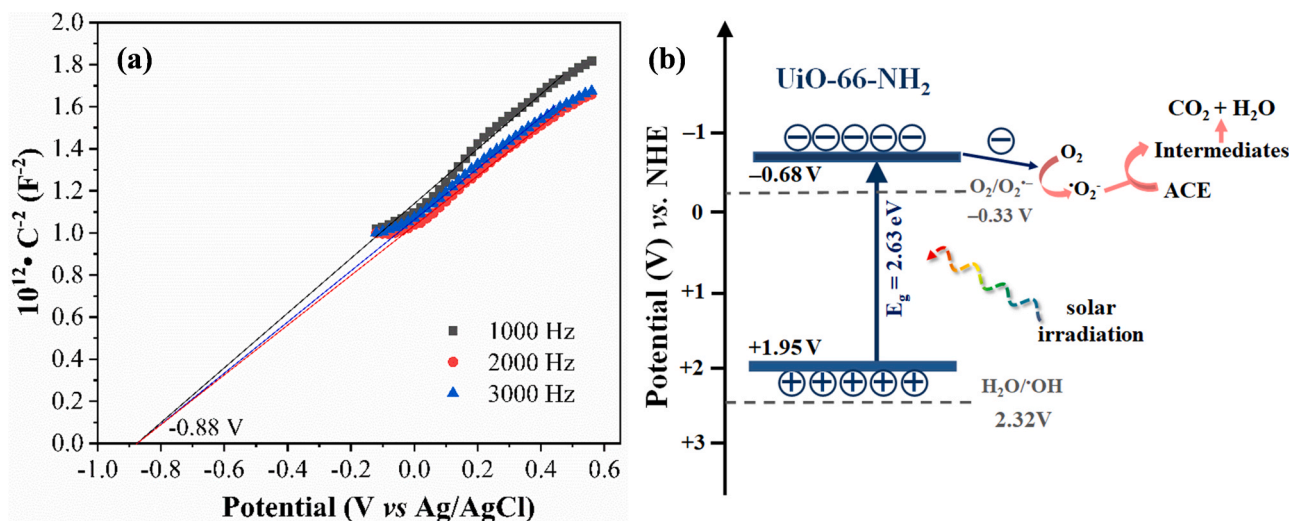


Fig. 9. (a) Mott-Schottky plots of UiO-66-NH<sub>2</sub> at 1000, 2000 and 3000 Hz in 0.1 M Na<sub>2</sub>SO<sub>4</sub> aqueous solution, and (b) electronic band structure of UiO-66-NH<sub>2</sub>.

photoactivity include not only the capture and recombination of photo-generated electron holes but also the crystallinity, morphology, and textural properties. In this sense, the better photocatalytic activity of UiO-66-NH<sub>2</sub> can be due to its significantly more developed porosity, higher surface area and higher crystallinity compared to UiO-66-(OH)<sub>2</sub>. Regarding crystallinity, the crystal size of the UiO-66-(OH)<sub>2</sub> is one-half that of UiO-66-NH<sub>2</sub>, which implies the presence of a greater number of defects that can entrap the electron-hole pairs impairing the reaction [48,49].

The reactive species responsible of the photo-assisted oxidation of ACE can include superoxide and hydroxyl radicals together with electrons and/or holes. To learn on the role of these reactive species on ACE degradation with the UiO-66-NH<sub>2</sub> photocatalyst, experiments were conducted with different scavengers, such as p-benzoquinone (p-BQ), 2-propanol, AgNO<sub>3</sub> and triethylamine (TEA) as trapping reagents for superoxide radicals ( $\cdot\text{O}_2^-$ ), hydroxyl radicals ( $\cdot\text{OH}$ ), electrons ( $e^-$ ) and holes ( $h^+$ ), respectively. The initial concentration of these scavengers was set at 1 mM. Fig. 8 shows the time-evolution of ACE in the presence of the different scavengers. The inhibitory effect of TEA is very weak, indicating that holes must not play a significant role in the degradation process. Similar situations were observed with 2-propanol and AgNO<sub>3</sub>, thus suggesting negligible contribution of  $\cdot\text{OH}$  and no direct reaction with  $e^-$ . However, the activity of UiO-66-NH<sub>2</sub> is greatly suppressed by p-BQ, so that superoxide radicals ( $\cdot\text{O}_2^-$ ) appear the most likely reactive species in ACE degradation. It has been reported that the photocatalytic degradation of ACE over TiO<sub>2</sub>-based materials proceeds mainly through hydroxyl radical ( $\cdot\text{OH}$ ) [50,51], although superoxide radicals ( $\cdot\text{O}_2^-$ ) have been claimed as the main contributing species with non-TiO<sub>2</sub> photocatalysts [44,45,52].

To elucidate the radical mechanism involved in the photo-degradation of ACE, Mott-Schottky measurements on UiO-66-NH<sub>2</sub> were conducted at different frequencies and the band structure was established (Fig. 9). The positive slope of  $C^{-2}$  vs. potential plot is consistent with a typical n-type semiconductor [53,54], being its conduction potential 0.2 V lower than the flat band determined by extrapolating the slope to the X-axis [55]. According to the intersection point, the conduction band minimum (CBM) of UiO-66-NH<sub>2</sub> is located at -0.68 V, similar to the reported in pervious works [56,57], and the valence band maximum (VBM) at 1.95 V vs. NHE, determined from the band gap previously calculated ( $E_{\text{CBM}} = E_{\text{VBM}} - E_g$ ). By irradiation, the electrons migrate from the BV to CB, resulting in photo-generated electrons ( $e^-$ ) and holes ( $h^+$ ). Since the CBM of UiO-66-NH<sub>2</sub> is more negative than the standard redox potential of superoxide radicals ( $E(\text{O}_2/\cdot\text{O}_2^-) = -0.33 \text{ V}$  vs. NHE) [58], the  $e^-$  can react with oxygen to generate the  $\cdot\text{O}_2^-$  radicals

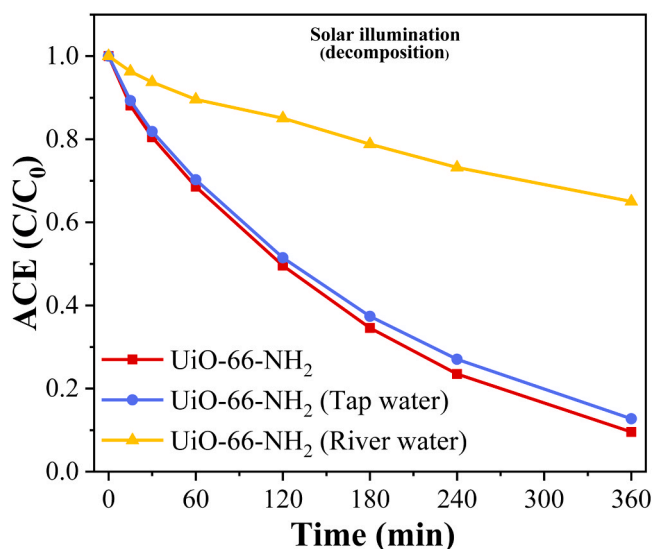


Fig. 10. Photocatalytic degradation of acetaminophen carried out in deionized, tap, and river water upon solar light.

responsible of ACE degradation. Moreover, the VBM is lower than the standard redox potential of hydroxyl radicals ( $E(\text{H}_2\text{O}/\cdot\text{OH}) = 2.40 \text{ V}$  vs. NHE) [59], so that the  $\cdot\text{OH}$  cannot be generated and therefore are not involved in the reaction, in agreement with the scavenger tests.

In addition, regarding potential application, the photocatalytic degradation of ACE from river and tap water as natural water samples was investigated. As shown in Fig. 10, the use of UiO-66-NH<sub>2</sub> as photocatalyst led to similar ACE conversion in deionized and tap water samples, so it can be inferred that the presence of inorganic ions has little effect on photocatalytic performance. However, the activity of UiO-66-NH<sub>2</sub> was inhibited in river water, which may be related to the more complex natural organic matter or the influence of the humic matter. This is consistent with previous research results [60,61].

To learn on the stability of the UiO-66-NH<sub>2</sub>, its performance was checked in a 30 h continuous flow test, being the experimental set-up schematized in Fig. S2. Fresh ACE solution ( $5 \text{ mg L}^{-1}$ ) was continuously fed to the reactor at  $0.7 \text{ mL min}^{-1}$ . The concentration of photocatalyst was  $250 \text{ mg L}^{-1}$ . Catalyst loss in the stream was conveniently prevented by a filter device in the outlet. Fig. 11 shows the evolution of ACE upon time on stream. Once the steady state was reached ( $\approx 3 \text{ h}$ ) the

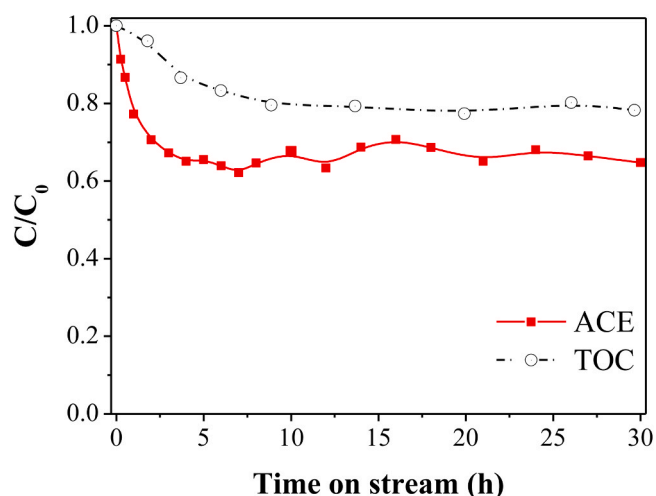


Fig. 11. Evolution of ACE and TOC upon time on stream in continuous experiment with UiO-66-NH<sub>2</sub> ([ACE]<sub>0</sub> = 5 mg L<sup>-1</sup>; [catalyst] = 250 mg L<sup>-1</sup>; flow = 0.7 mL min<sup>-1</sup>; Intensity = 600 W m<sup>-2</sup>).

photocatalytic performance was maintained almost constant during the whole experiment. TOC reduction (Fig. 11) described a similar trend, with a less steep slope at the beginning of the test, achieving a stable

steady state TOC reduction. The absence of 2ATA (organic ligand) in the outlet solution during the whole test was confirmed by chromatography, supporting the stability of the photocatalyst under the reaction conditions of the long-term continuous experiment. The stability of the UiO-66-NH<sub>2</sub> upon continuous operation was confirmed by FTIR, analyzing the photocatalyst recovered after the 30 h on stream (Fig. S3). The bands at 1680 and 1270 cm<sup>-1</sup> associated, respectively, to the N—H bending and C—N stretching vibrations, were still evident in the spectrum, demonstrating that no changes on the functional group occurred after continuous operation.

### 3.3. ACE degradation byproducts and reaction pathway

The degradation pathway of ACE with UiO-66-NH<sub>2</sub> was investigated by LC/ESI-MS and IC. The accurate mass and the assessment of detected species can be seen in Table S1 and the proposed degradation pathway is depicted in Fig. 12. ACE molecules can interact with each other at either the ortho or amide bonding positions coupling into dimer (ACE-1; *m/z*: 301.1181) and trimer (ACE-2; *m/z*: 450.1661). These byproducts were previously detected by our group in the degradation of ACE with TiO<sub>2</sub>-activated carbon heterostructures [42]. Additionally, acetaminophen aromatic ring can be oxidized without ring cleavage, resulting in the formation of ACE-3 byproduct (*m/z*: 168.0653). The ring-opening of ACE and ACE-3 can lead to the formation of different types of carboxylic acids, such as the detected malonic and oxalic acids. Further oxidation of

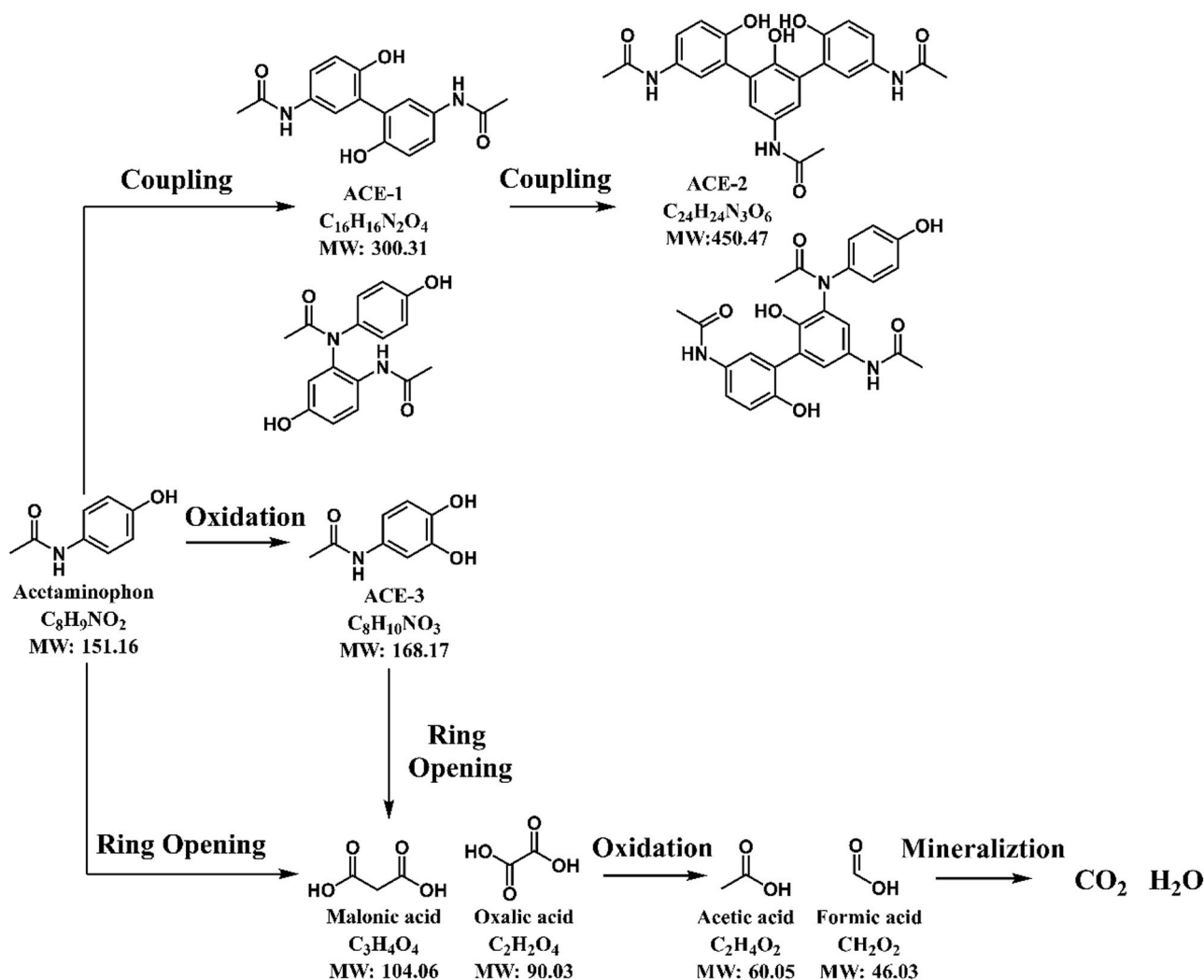
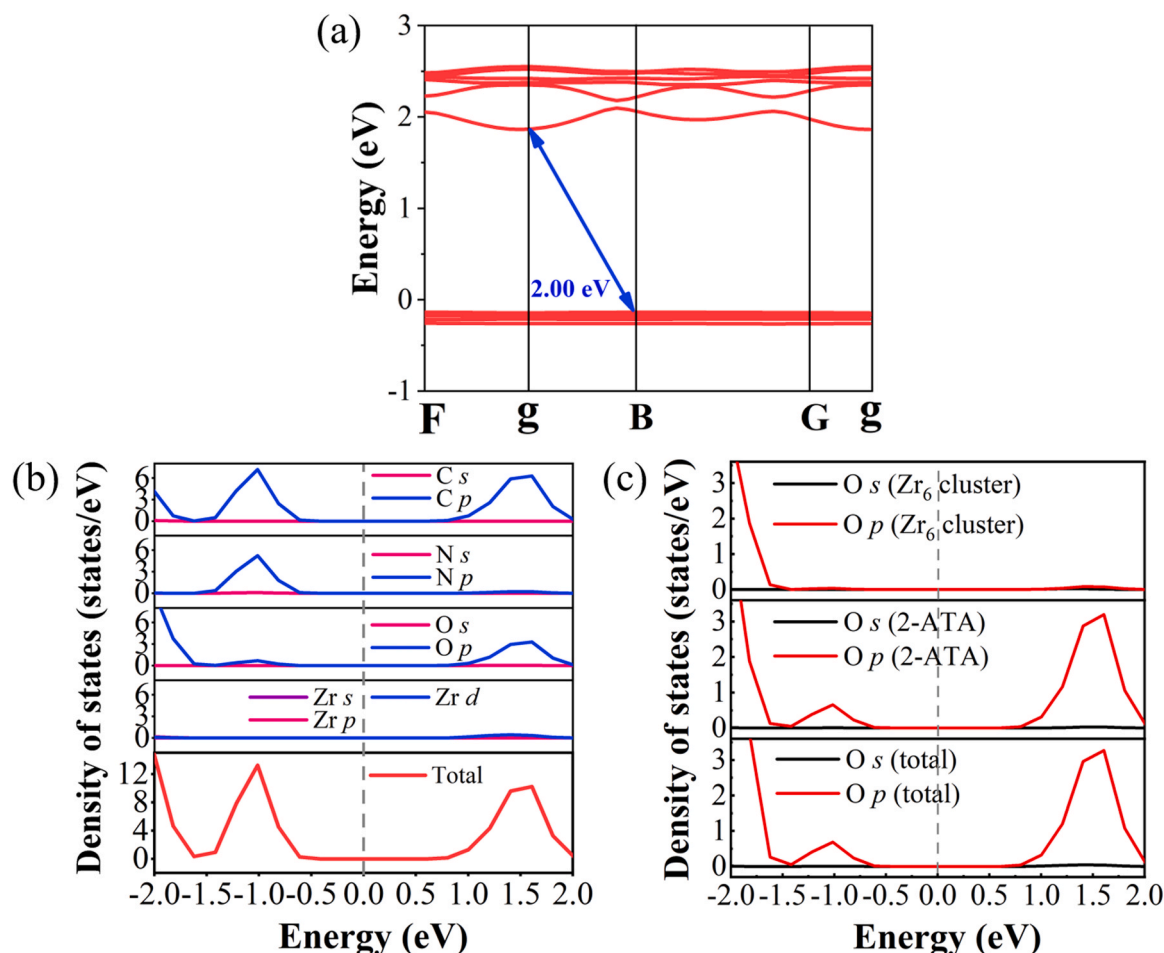


Fig. 12. Proposed degradation pathway of ACE with the UiO-66-NH<sub>2</sub> photocatalyst under solar irradiation.





**Fig. 13.** (a) Electronic band structures of UiO-66-NH<sub>2</sub> calculated by the DFT-PBE method; (b) total and orbital-projected partial density of states of UiO-66-NH<sub>2</sub>; (c) partial density of oxygen states from Zr<sub>6</sub> cluster and ligand.

these last gives rise to acetic and formic acids. Eventually, CO<sub>2</sub> and H<sub>2</sub>O are formed as final mineralization products.

### 3.4. Density functional theory calculation

Valence band maximum (VBM) and conduction band minimum (CBM) are one of the important indicators to evaluate the performance of photocatalytic materials. The distribution of density of states (DOS) can clarify the electron migration path of the MOF photocatalyst. Therefore, it is necessary to gain the energy band structure and density of states of the photocatalyst through first-principle density functional theory (DFT) in order to deeply explore the photocatalytic behavior of charge carrier in the photocatalyst. To learn more on how functionalization effects to the electronic structure of the UiO-66-NH<sub>2</sub>, calculations of the electronic band structure and DOS were performed with the assistance of MedaA & VASP software as illustrated in Figs. 13, S4 and S5. The abscissa of Fig. 13a represents the special *k* points in the first Brillouin zone. It can be observed that the valence band maximum (VBM) locates at the B point while the conduction band minimum (CBM) at the g point, forming an indirect band gap with an estimated value of 2.13 eV where the VBM and CBM are located at −0.136 and 1.999 eV, respectively, with respect to the Fermi level. However, the band gap measured by Tauc Plot was considerably higher (2.64 eV) than this estimated value. It is well known that GGA-PBE approximation underestimates band gap values, but here, we are interested in the general structure of the band gap rather than the absolute values. Generally, for indirect band gap semiconductors, the path of photoinduced electron-hole pair separation and transfer is longer compared to the direct case, but the

recombination rate of photoinduced charges would be reduced simultaneously. The reduced combination rate of electron and hole in indirect semiconductors is beneficial to photocatalysis [62]. The electron localization function (ELF) characterizes the localized distribution of electrons (Fig. S4), where red and blue represent fully localized and delocalized (almost no localized) electrons, and the part with a value of 0.5 in green corresponds to the distribution of electron-gas-like pairs [63]. We observed that the electrons are greatly localized in the regions covering the holistic 2ATA, which illustrates the existence of a strong covalent bond (delocalized  $\pi$  bond). It can be seen from Fig. S4 that the excited electrons are moving around the whole ligand in both TA of UiO-66 and 2ATA of UiO-66-NH<sub>2</sub>. Electrons in 2ATA have a larger area of movement than in TA, so that charge transfer is more favorable, resulting in higher photocatalytic performance.

The calculated total and orbital-resolved partial densities of states (PDOS) of UiO-66-NH<sub>2</sub> are summarized in Fig. 13b. PDOS reveals that the electronic states of the valence band near the Fermi level are dominated by C *p*, N *p* and fractionally derived from O *p* orbitals, while the conduction band close to the Fermi level mainly originates from the C *p*, O *p* and slightly Zr *p* orbitals. It can be inferred that the direction of electrons migration is mainly from C—N bond to C—O bond. In addition, the non-dispersive (flat) VB contributed by C *p* and N *p* indicates that the electrons of the ligand at the ground state are localized [64]. Hence, intermolecular coupling between the 2ATA ligands does not occur. This is consistent with the structure of UiO-66, demonstrating that the structure of UiO-66-NH<sub>2</sub> is cognate with that of UiO-66. The results of DOS of UiO-66-NH<sub>2</sub> confirm the above discussions on the ELF; the electrons are basically distributed in the ligand rather than in the Zr



metal cluster. The carbon and nitrogen states are located in aromatic ligand carbons and amino group, as well as the oxygen states correspond mostly to carboxylate groups and only slightly to Zr-O<sub>μ3-O</sub> (Fig. 13c), implying that both the VB and CB are mainly located on 2ATA ligand, as previously reported by Zeama et al. [65]. Given the small contribution of Zr<sub>4</sub><sup>+</sup> to CB and VB, it may be reasonably concluded that the photocatalytic performance is determined mainly by the 2ATA ligand rather than Zr<sub>4</sub><sup>+</sup>. Based on these results, a ligand-to-ligand charge transfer (LLCT) appears more likely to occur in UiO-66-NH<sub>2</sub>.

#### 4. Conclusions

The activity of UiO-66-based photocatalysts for acetaminophen degradation is significantly influenced by the presence of different types of functional groups in the organic ligands of the MOF. UiO-66-NH<sub>2</sub> showed the best performance in ACE photocatalytic degradation since it combines great crystallinity, high specific surface area, low photo-generated electron recombination rate, better charge mobility and stability in water. It can be concluded that superoxide radicals (<sup>•</sup>O<sub>2</sub><sup>-</sup>) acted as the major reactive species in acetaminophen photodegradation with UiO-66-NH<sub>2</sub>. In continuous flow test, stable conversion of ACE was reached after 3 h on stream and then maintained for the rest of the 30 h experiment. This, besides the absence of organic ligand leaching to the aqueous phase, are indicative of the good stability of that MOF, a promising issue regarding potential application. In the proposed degradation pathway includes acetaminophen coupling into dimers and trimers, ring-opening reactions, and mineralization. DFT calculation supports the indirect semiconductor behavior of UiO-66-NH<sub>2</sub>, and the DOS results indicate that light excitation occurs through ligand-ligand charge transfer (LLCT). Thus, the photocatalytic performance is mainly determined by the functionalized ligand rather than the zirconium cluster.

#### CRedit authorship contribution statement

The manuscript was written through contributions of all authors. All authors have given approval to the final version of the manuscript.

#### Supporting Information

Supporting information provides additional figures and tables to support the discussion of results.

#### Declaration of Competing Interest

The authors declare that they have no known competing financial interests or personal relationships that could have appeared to influence the work reported in this paper.

#### Acknowledgments

This research was funded by the National State Research Agency of Spain (project number: PID2019-106186RB-I00/AEI/10.13039/501100011033). Yilan Wang acknowledges the support from the China Scholarship Council (CSC No. 201908610198). We also thank to Prof. Shi Ye for his help with density functional theory calculation.

#### Appendix A. Supporting information

Supplementary data associated with this article can be found in the online version at [doi:10.1016/j.jece.2021.106087](https://doi.org/10.1016/j.jece.2021.106087).

#### References

- [1] Q. Wang, Q. Gao, A.M. Al-Enizi, A. Nafady, S. Ma, Recent advances in MOF-based photocatalysis: environmental remediation under visible light, *Inorg. Chem. Front.* 7 (2020) 300–339, <https://doi.org/10.1039/c9qi01120j>.
- [2] H.N. Phong Vo, G.K. Le, T.M. Hong Nguyen, X.T. Bui, K.H. Nguyen, E.R. Rene, T.D. H. Vo, N.D. Thanh Cao, R. Mohan, Acetaminophen micropollutant: historical and current occurrences, toxicity, removal strategies and transformation pathways in different environments, *Chemosphere* 236 (2019), 124391, <https://doi.org/10.1016/j.chemosphere.2019.124391>.
- [3] T.X.H. Le, T. Van Nguyen, Z. Amadou Yacoubia, L. Zounggrana, F. Avril, D. L. Nguyen, E. Petit, J. Mendret, V. Bonniol, M. Bechelany, S. Lacour, G. Lesage, M. Cretin, Correlation between degradation pathway and toxicity of acetaminophen and its by-products by using the electro-Fenton process in aqueous media, *Chemosphere* 172 (2017) 1–9, <https://doi.org/10.1016/j.chemosphere.2016.12.060>.
- [4] Q.C. Do, D.G. Kim, S.O. Ko, Nonsacrificial template synthesis of magnetic-based yolk-shell nanostructures for the removal of acetaminophen in fenton-like systems, *ACS Appl. Mater. Interfaces* 9 (2017) 28508–28518, <https://doi.org/10.1021/acsami.7b07658>.
- [5] Y. Zhang, Q. Zhang, J. Hong, Sulfate radical degradation of acetaminophen by novel iron–copper bimetallic oxidation catalyzed by persulfate: mechanism and degradation pathways, *Appl. Surf. Sci.* 422 (2017) 443–451, <https://doi.org/10.1016/j.apsusc.2017.05.224>.
- [6] A. Gómez-Avilés, M. Peñas-Garzón, J. Bedia, J.J. Rodríguez, C. Belver, C-modified TiO<sub>2</sub> using lignin as carbon precursor for the solar photocatalytic degradation of acetaminophen, *Chem. Eng. J.* 358 (2019) 1574–1582, <https://doi.org/10.1016/j.cej.2018.10.154>.
- [7] A. Gómez-Avilés, L. Sellaoui, M. Badawi, A. Bonilla-Petriciolet, J. Bedia, C. Belver, Simultaneous adsorption of acetaminophen, diclofenac and tetracycline by organo-sepiolite: experiments and statistical physics modelling, *Chem. Eng. J.* 404 (2021), 126601, <https://doi.org/10.1016/j.cej.2020.126601>.
- [8] V.K. Sharma, M. Feng, Water depollution using metal-organic frameworks-catalyzed advanced oxidation processes: a review, *J. Hazard. Mater.* 372 (2019) 3–16, <https://doi.org/10.1016/j.jhazmat.2017.09.043>.
- [9] H. Dong, G. Zeng, L. Tang, C. Fan, C. Zhang, X. He, Y. He, An overview on limitations of TiO<sub>2</sub>-based particles for photocatalytic degradation of organic pollutants and the corresponding countermeasures, *Water Res.* 79 (2015) 128–146, <https://doi.org/10.1016/j.watres.2015.04.038>.
- [10] Y. Gao, J. Xia, D. Liu, R. Kang, G. Yu, S. Deng, Synthesis of mixed-linker Zr-MOFs for emerging contaminant adsorption and photodegradation under visible light, *Chem. Eng. J.* 378 (2019), 122118, <https://doi.org/10.1016/j.cej.2019.122118>.
- [11] L. He, Y. Dong, Y. Zheng, Q. Jia, S. Shan, Y. Zhang, A novel magnetic MIL-101(Fe)/TiO<sub>2</sub> composite for photo degradation of tetracycline under solar light, *J. Hazard. Mater.* 361 (2019) 85–94, <https://doi.org/10.1016/j.jhazmat.2018.08.079>.
- [12] N. Li, X. Liu, J. Zhou, W. Chen, M. Liu, Encapsulating CuO quantum dots in MIL-125(Ti) coupled with g-C<sub>3</sub>N<sub>4</sub> for efficient photocatalytic CO<sub>2</sub> reduction, *Chem. Eng. J.* 399 (2020), 125782, <https://doi.org/10.1016/j.cej.2020.125782>.
- [13] R. Wang, L. Gu, J. Zhou, X. Liu, F. Teng, C. Li, Y. Shen, Y. Yuan, Quasi-Polymeric Metal-Organic Framework UiO-66/g-C<sub>3</sub>N<sub>4</sub> heterojunctions for enhanced photocatalytic hydrogen evolution under visible light irradiation, *Adv. Mater. Interfaces* 2 (2015), 1500037, <https://doi.org/10.1002/admi.201500037>.
- [14] S. Ali Akbar Razavi, A. Morsali, Linker functionalized metal-organic frameworks, *Coord. Chem. Rev.* 399 (2019), 213023, <https://doi.org/10.1016/j.ccr.2019.213023>.
- [15] J. Bedia, V. Muelas-Ramos, M. Peñas-Garzón, A. Gómez-Avilés, J.J. Rodríguez, C. Belver, A review on the synthesis and characterization of metal organic frameworks for photocatalytic water purification, *Catalysts* 9 (2019) 52, <https://doi.org/10.3390/catal9010052>.
- [16] A. Gómez-Avilés, V. Muelas-Ramos, J. Bedia, J.J. Rodríguez, C. Belver, Thermal post-treatments to enhance the water stability of NH<sub>2</sub>-MIL-125(Ti), *Catalysts* 10 (2020) 603, <https://doi.org/10.3390/catal10060603>.
- [17] X. Liu, N.K. Demir, Z. Wu, K. Li, Highly water-stable Zirconium Metal-Organic Framework UiO-66 membranes supported on alumina hollow fibers for desalination, *J. Am. Chem. Soc.* 137 (2015) 6999–7002, <https://doi.org/10.1021/jacs.5b02276>.
- [18] Y. Zhang, J. Zhou, Q. Feng, X. Chen, Z. Hu, Visible light photocatalytic degradation of MB using UiO-66/g-C<sub>3</sub>N<sub>4</sub> heterojunction nanocatalyst, *Chemosphere* 212 (2018) 523–532, <https://doi.org/10.1016/j.chemosphere.2018.08.117>.
- [19] T.F. Chen, S.Y. Han, Z.P. Wang, H. Gao, L.Y. Wang, Y.H. Deng, C.Q. Wan, Y. Tian, Q. Wang, G. Wang, G.S. Li, Modified UiO-66 frameworks with methylthio, thiol and sulfonic acid function groups: the structure and visible-light-driven photocatalytic property study, *Appl. Catal. B Environ.* 259 (2019), 118047, <https://doi.org/10.1016/j.apcatb.2019.118047>.
- [20] X. Mu, J. Jiang, F. Chao, Y. Lou, J. Chen, Ligand modification of UiO-66 with an unusual visible light photocatalytic behavior for RhB degradation, *Dalton Trans.* 47 (2018) 1895–1902, <https://doi.org/10.1039/c7dt04477a>.
- [21] A. Nandy, A.C. Forse, V.J. Witherspoon, J.A. Reimer, NMR Spectroscopy reveals adsorbate binding sites in the Metal-Organic Framework UiO-66(Zr), *J. Phys. Chem. C* 122 (2018) 8295–8305, <https://doi.org/10.1021/acs.jpcc.7b12628>.
- [22] L. Liu, W. Cui, C. Lu, A. Zain, W. Zhang, G. Shen, S. Hu, X. Qian, Analyzing the adsorptive behavior of Amoxicillin on four Zr-MOFs nanoparticles: functional groups dependence of adsorption performance and mechanisms, *J. Environ. Manag.* 268 (2020), 110630, <https://doi.org/10.1016/j.jenvman.2020.110630>.
- [23] D.F. Sava Gallis, J.A. Harvey, C.J. Pearce, M.G. Hall, J.B. DeCoste, M.K. Kinnan, J. A. Greathouse, Efficient MOF-based degradation of organophosphorus compounds

- in non-aqueous environments, *J. Mater. Chem. A* 6 (2018) 3038–3045, <https://doi.org/10.1039/c7ta10794c>.
- [24] H.R. Abid, H.M. Ang, S. Wang, Effects of ammonium hydroxide on the structure and gas adsorption of nanosized Zr-MOFs (UiO-66), *Nanoscale* 4 (2012) 3089–3094, <https://doi.org/10.1039/c2nr30244f>.
- [25] S. Chen, J. Liu, Y. Xu, Z. Li, T. Wang, J. Xu, Z. Wang, Hydrogen storage properties of the novel crosslinked UiO-66-(OH)<sub>2</sub>, *Int. J. Hydrog. Energy* 43 (2018) 15370–15377, <https://doi.org/10.1016/j.ijhydene.2018.06.106>.
- [26] W. Zhao, T. Ding, Y. Wang, M. Wu, W. Jin, Y. Tian, X. Li, Decorating Ag/AgCl on UiO-66-NH<sub>2</sub>: synergy between Ag plasmons and heterostructure for the realization of efficient visible light photocatalysis, *Chin. J. Catal.* 40 (2019) 1187–1197, [https://doi.org/10.1016/S1872-2067\(19\)63377-2](https://doi.org/10.1016/S1872-2067(19)63377-2).
- [27] C.S. Yan, H.Y. Gao, L. Le Gong, L.F. Ma, L.L. Dang, L. Zhang, P.P. Meng, F. Luo, MOF surface method for the ultrafast and one-step generation of metal-oxide-NP@MOF composites as lithium storage materials, *J. Mater. Chem. A* 4 (2016) 13603–13610, <https://doi.org/10.1039/c6ta03687b>.
- [28] H. Xie, D. Ma, W. Liu, Q. Chen, Y. Zhang, J. Huang, H. Zhang, Z. Jin, T. Luo, F. Peng, Zr-Based MOFs as new photocatalysts for the rapid reduction of Cr(vi) in water, *New J. Chem.* 44 (2020) 7218–7225, <https://doi.org/10.1039/d0nj00457j>.
- [29] M. Sarker, H.J. An, S.H. Jhung, Adsorptive removal of indole and quinoline from model fuel over various UiO-66s: quantitative contributions of h-bonding and acid-base interactions to adsorption, *J. Phys. Chem. C* 122 (2018) 4532–4539, <https://doi.org/10.1021/acs.jpcc.8b00761>.
- [30] J. Noh, Y. Kim, H. Park, J. Lee, M. Yoon, M.H. Park, Y. Kim, M. Kim, Functional group effects on a metal-organic framework catalyst for CO<sub>2</sub> cycloaddition, *J. Ind. Eng. Chem.* 64 (2018) 478–483, <https://doi.org/10.1016/j.jiec.2018.04.010>.
- [31] C. Chen, D. Chen, S. Xie, H. Quan, X. Luo, L. Guo, Adsorption behaviors of organic micropollutants on Zirconium Metal-Organic Framework UiO-66: analysis of surface interactions, *ACS Appl. Mater. Interfaces* 9 (2017) 41043–41054, <https://doi.org/10.1021/acsami.7b13443>.
- [32] Z. Wang, J. Yang, Y. Li, Q. Zhuang, J. Gu, Simultaneous degradation and removal of crvi from aqueous solution with Zr-Based Metal-Organic Frameworks bearing inherent reductive sites, *Chem. A Eur. J.* 23 (2017) 15415–15423, <https://doi.org/10.1002/chem.201702534>.
- [33] G.Y. Shang, P. Chammingkwan, D.X. Trinh, T. Taniike, Design of a semi-continuous selective layer based on deposition of UiO-66 nanoparticles for nanofiltration, *Membranes* 8 (2018) 129, <https://doi.org/10.3390/membranes8040129>.
- [34] J. Ding, Z. Yang, C. He, X. Tong, Y. Li, X. Niu, H. Zhang, UiO-66(Zr) coupled with Bi<sub>2</sub>MoO<sub>6</sub> as photocatalyst for visible-light promoted dye degradation, *J. Colloid Interface Sci.* 497 (2017) 126–133, <https://doi.org/10.1016/j.jcis.2017.02.060>.
- [35] Y. Han, M. Liu, K. Li, Y. Zuo, Y. Wei, S. Xu, G. Zhang, C. Song, Z. Zhang, X. Guo, Facile synthesis of morphology and size-controlled zirconium metal-organic framework UiO-66: the role of hydrofluoric acid in crystallization, *CrystEngComm* 17 (2015) 6434–6440, <https://doi.org/10.1039/c5ce00729a>.
- [36] P. Jia, K. Yang, J. Hou, Y. Cao, X. Wang, L. Wang, Ingenious dual-emitting Ru@UiO-66-NH<sub>2</sub> composite as ratiometric fluorescence sensor for detection of mercury in aqueous, *J. Hazard. Mater.* 408 (2021), 124469, <https://doi.org/10.1016/j.jhazmat.2020.124469>.
- [37] M. Kandiah, S. Usseglio, S. Svelle, U. Olsbye, K.P. Lillerud, M. Tilset, Post-synthetic modification of the metal-organic framework compound UiO-66, *J. Mater. Chem.* 20 (2010) 9848–9851, <https://doi.org/10.1039/c0jm02416c>.
- [38] Y. Sun, M. Chen, H. Liu, Y. Zhu, D. Wang, M. Yan, Adsorptive removal of dye and antibiotic from water with functionalized zirconium-based metal organic framework and graphene oxide composite nanomaterial UiO-66-(OH)<sub>2</sub>/GO, *Appl. Surf. Sci.* 525 (2020), 146614, <https://doi.org/10.1016/j.apsusc.2020.146614>.
- [39] F.A. Sofi, K. Majid, O. Mehraj, The visible light driven copper based metal-organic-framework heterojunction: HKUST-1@Ag-Ag<sub>3</sub>PO<sub>4</sub> for plasmon enhanced visible light photocatalysis, *J. Alloy. Compd.* 737 (2018) 798–808, <https://doi.org/10.1016/j.jallcom.2017.12.141>.
- [40] H. Zhang, Z. Yu, R. Jiang, Y. Hou, J. Huang, H. Zhu, F. Yang, M. Li, F. Li, Q. Ran, Metal organic frameworks constructed heterojunction with α-NiS-β-NiS/CdS: the effect of organic-ligand in UiO-66 for charge transfer of photocatalytic hydrogen evolution, *Renew. Energy* 168 (2021) 1112–1121, <https://doi.org/10.1016/j.renene.2020.12.102>.
- [41] M. Akkari, P. Aranda, C. Belver, J. Bedia, A. Ben Haj Amara, E. Ruiz-Hitzky, ZnO/sepiolite heterostructured materials for solar photocatalytic degradation of pharmaceuticals in wastewater, *Appl. Clay Sci.* 156 (2018) 104–109, <https://doi.org/10.1016/j.clay.2018.01.021>.
- [42] M. Peñas-Garzón, A. Gómez-Avilés, C. Belver, J.J. Rodríguez, J. Bedia, Degradation pathways of emerging contaminants using TiO<sub>2</sub>-activated carbon heterostructures in aqueous solution under simulated solar light, *Chem. Eng. J.* 392 (2020), 124867, <https://doi.org/10.1016/j.cej.2020.124867>.
- [43] M. Tobajas, C. Belver, J.J. Rodríguez, Degradation of emerging pollutants in water under solar irradiation using novel TiO<sub>2</sub>-ZnO/clay nanoarchitectures, *Chem. Eng. J.* 309 (2017) 596–606, <https://doi.org/10.1016/j.cej.2016.10.002>.
- [44] A. Gómez-Avilés, M. Peñas-Garzón, J. Bedia, D.D. Dionysiou, J.J. Rodríguez, C. Belver, Mixed Ti-Zr metal-organic-frameworks for the photodegradation of acetaminophen under solar irradiation, *Appl. Catal. B Environ.* 253 (2019) 253–262, <https://doi.org/10.1016/j.apcatb.2019.04.040>.
- [45] Z. Yang, X. Xu, X. Liang, C. Lei, L. Gao, R. Hao, D. Lu, Z. Lei, Fabrication of Ce doped UiO-66/graphene nanocomposites with enhanced visible light driven photoactivity for reduction of nitroaromatic compounds, *Appl. Surf. Sci.* 420 (2017) 276–285, <https://doi.org/10.1016/j.apsusc.2017.05.158>.
- [46] J.Z. Wei, F.X. Gong, X.J. Sun, Y. Li, T. Zhang, X.J. Zhao, F.M. Zhang, Rapid and low-cost electrochemical synthesis of UiO-66-NH<sub>2</sub> with enhanced fluorescence detection performance, *Inorg. Chem.* 58 (2019) 6742–6747, <https://doi.org/10.1021/acs.inorgchem.9b00157>.
- [47] C. Yao, Y. Xu, Z. Xia, A carbon dot-encapsulated UiO-type metal organic framework as a multifunctional fluorescent sensor for temperature, metal ion and pH detection, *J. Mater. Chem. C* 6 (2018) 4396–4399, <https://doi.org/10.1039/c8tc01018h>.
- [48] G. Colón-Ibáñez, C. Belver-Coldeira, M. Fernández-García, Nanostructured oxides in photo-catalysis, *Synth. Prop. Appl. Oxide Nanomater*, John Wiley & Sons, Inc, 2006, pp. 491–562, <https://doi.org/10.1002/9780470108970.ch17>.
- [49] M. Bellardita, A. Di Paola, B. Megna, L. Palmisano, Absolute crystallinity and photocatalytic activity of brookite TiO<sub>2</sub> samples, *Appl. Catal. B Environ.* 201 (2017) 150–158, <https://doi.org/10.1016/j.apcatb.2016.08.012>.
- [50] R. Mu, Y. Ao, T. Wu, C. Wang, P. Wang, Synthesis of novel ternary heterogeneous anatase-TiO<sub>2</sub> (B) biphasic nanowires/Bi<sub>2</sub>O<sub>3</sub>/I<sub>2</sub> composite photocatalysts for the highly efficient degradation of acetaminophen under visible light irradiation, *J. Hazard. Mater.* 382 (2020), 121083, <https://doi.org/10.1016/j.jhazmat.2019.121083>.
- [51] X. Feng, P. Wang, J. Hou, J. Qian, C. Wang, Y. Ao, Oxygen vacancies and phosphorus codoped black titania coated carbon nanotube composite photocatalyst with efficient photocatalytic performance for the degradation of acetaminophen under visible light irradiation, *Chem. Eng. J.* 352 (2018) 947–956, <https://doi.org/10.1016/j.cej.2018.06.037>.
- [52] L.K.B. Paragas, V. Dien Dang, R.S. Sahu, S. Garcia-Segura, M.D.G. de Luna, J.A. I. Pimentel, R.A. Doong, Enhanced visible-light-driven photocatalytic degradation of acetaminophen over CeO<sub>2</sub>/I<sub>2</sub> K-codoped C<sub>3</sub>N<sub>4</sub> heterojunction with tunable properties in simulated water matrix, *Sep. Purif. Technol.* 272 (2021), 117567, <https://doi.org/10.1016/j.seppur.2020.117567>.
- [53] S. Subudhi, L. Paramanik, S. Sultana, S. Mansingh, P. Mohapatra, K. Parida, A type-II interband alignment heterojunction architecture of cobalt titanate integrated Norfloxacin degradation and green energy (Hydrogen) evolution, *J. Colloid Interface Sci.* 568 (2020) 89–105, <https://doi.org/10.1016/j.jcis.2020.02.043>.
- [54] Q. Liang, S. Cui, C. Liu, S. Xu, C. Yao, Z. Li, Construction of CdS@UiO-66-NH<sub>2</sub> core-shell nanorods for enhanced photocatalytic activity with excellent photostability, *J. Colloid Interface Sci.* 524 (2018) 379–387, <https://doi.org/10.1016/j.jcis.2018.03.114>.
- [55] K. Sun, M. Liu, J. Pei, D. Li, C. Ding, K. Wu, H.L. Jiang, Incorporating transition-metal phosphides into Metal-Organic Frameworks for enhanced photocatalysis, *Angew. Chem. Int. Ed.* 59 (2020) 22749–22755, <https://doi.org/10.1002/anie.202011614>.
- [56] Y.F. Chen, L.L. Tan, J.M. Liu, S. Qin, Z.Q. Xie, J.F. Huang, Y.W. Xu, L.M. Xiao, C. Y. Su, Calix[4]arene based dye-sensitized Pt@UiO-66-NH<sub>2</sub> metal-organic framework for efficient visible-light photocatalytic hydrogen production, *Appl. Catal. B Environ.* 206 (2017) 426–433, <https://doi.org/10.1016/j.apcatb.2017.01.040>.
- [57] Y.X. Li, X. Wang, C.C. Wang, H. Fu, Y. Liu, P. Wang, C. Zhao, S-TiO<sub>2</sub>/UiO-66-NH<sub>2</sub> composite for boosted photocatalytic Cr(VI) reduction and bisphenol A degradation under LED visible light, *J. Hazard. Mater.* 399 (2020), 123085, <https://doi.org/10.1016/j.jhazmat.2020.123085>.
- [58] L. Shi, L. Yang, H. Zhang, K. Chang, G. Zhao, T. Kako, J. Ye, Implantation of Iron (III) in porphyrinic metal organic frameworks for highly improved photocatalytic performance, *Appl. Catal. B Environ.* 224 (2018) 60–68, <https://doi.org/10.1016/J.APCATB.2017.10.033>.
- [59] X. Li, J. Yu, M. Jaroniec, Hierarchical photocatalysts, *Chem. Soc. Rev.* 45 (2016) 2603–2636, <https://doi.org/10.1039/c5cs00838g>.
- [60] J. Liu, C. Li, R. Qu, J. Feng, L. Wang, Formation of perfluorocarboxylic acids from photodegradation of tetrahydroperfluorocarboxylic acids in water, *Sci. Total Environ.* 655 (2019) 598–606, <https://doi.org/10.1016/j.scitotenv.2018.11.231>.
- [61] N. Solomou, M. Minella, D. Vione, E. Psillakis, UVC-induced degradation of cilastatin in natural water and treated wastewater, *Chemosphere* 280 (2021), 130668, <https://doi.org/10.1016/j.chemosphere.2021.130668>.
- [62] J.K. Cooper, S. Gul, F.M. Toma, L. Chen, Y.S. Liu, J. Guo, J.W. Ager, J. Yano, I. D. Sharp, Indirect bandgap and optical properties of monoclinic bismuth vanadate, *J. Phys. Chem. C* 119 (2015) 2969–2974, <https://doi.org/10.1021/jp512169w>.
- [63] X. Lv, W. Wei, Q. Sun, F. Li, B. Huang, Y. Dai, Two-dimensional germanium monochalcogenides for photocatalytic water splitting with high carrier mobility, *Appl. Catal. B Environ.* 217 (2017) 275–284, <https://doi.org/10.1016/j.apcatb.2017.05.087>.
- [64] G. Wang, Q. Sun, Y. Liu, B. Huang, Y. Dai, X. Zhang, X. Qin, A bismuth-based metal-organic framework as an efficient visible-light-driven photocatalyst, *Chem. A Eur. J.* 21 (2015) 2364–2367, <https://doi.org/10.1002/chem.201405047>.
- [65] M. Zeama, M. Morsy, S. Abdel-Azeim, M. Abdelnaby, A. Allouh, Z. Yamani, Photophysical and photocatalytic properties of structurally modified UiO-66, *Inorg. Chim. Acta* 501 (2020), 119287, <https://doi.org/10.1016/j.ica.2019.119287>.